Fusion of autoradiographies with an MR volume using 2-D and 3-D linear transformations

Éric Bardinet, Grégoire Malandain

To cite this version:

Éric Bardinet, Grégoire Malandain. Fusion of autoradiographies with an MR volume using 2-D and 3-D linear transformations. RR-4791, INRIA. 2003. inria-00071795

HAL Id: inria-00071795
https://inria.hal.science/inria-00071795v1

Submitted on 23 May 2006

HAL is a multi-disciplinary open access archive for the deposit and dissemination of scientific research documents, whether they are published or not. The documents may come from teaching and research institutions in France or abroad, or from public or private research centers.

L'archive ouverte pluridisciplinaire **HAL**, est destinée au dépôt et à la diffusion de documents scientifiques de niveau recherche, publiés ou non, émanant des établissements d'enseignement et de recherche français ou étrangers, des laboratoires publics ou privés.

INSTITUT NATIONAL DE RECHERCHE EN INFORMATIQUE ET EN AUTOMATIQUE

Fusion of autoradiographies with an MR volume using 2-D and 3-D linear transformations

Éric Bardinet — Grégoire Malandain

N° 4791

March 26, 2003

THÈME 3

Rapport de recherche

ISSN 0249-6399 ISRN INRIA/RR--4791--FR+ENG

INRIA
SOPHIA ANTIPOLIS

Fusion of autoradiographies with an MR volume using 2-D and 3-D linear transformations

Éric Bardinet* , Grégoire Malandain

Thème 3 — Interaction homme-machine,
images, données, connaissances
Projet Epidaure

Rapport de recherche n° 4791 — March 26, 2003 — 33 pages

Abstract: In the past years, the development of 3-D medical imaging devices has given access to the 3-D imaging of *in vivo* tissues, from an anatomical (MR, CT) or even functional point of view (fMRI, PET, SPECT). However, despite huge technological progress, the resolution of these images is still not sufficient to image to anatomical or functional details, that can only be revealed by *in vitro* imaging (e.g. histology, autoradiography), eventually enhanced by staining.

The deep motivation of this work is the comparison of activations detected by fMRI series analysis to the ones that can be observed in autoradiographic images. The aim of the presented work is to fuse the autoradiographic data with the pre-mortem anatomical MR image, to facilitate the above mentioned comparison.

First, we reconstruct a 3-D volume, coherent both in geometry and intensity, from the 2-D autoradiographic sections. Second, this volume is fused with the MR image, that allows to geometrically correct the reconstruction to make it comparable to the MR image.

We show that this fusion can be achieved by using only simple global transformations (rigid and/or affine, 2-D and 3-D), yielding a very satisfactory result.

Key-words: Fusion, reconstruction, autoradiography, MRI

---

* Éric Bardinet is now with CNRS UPR 640 - LENA, hôpital La Pitié-Salpétrière, Paris.

Unité de recherche INRIA Sophia Antipolis
2004, route des Lucioles, BP 93, 06902 Sophia Antipolis Cedex (France)
Téléphone : +33 4 92 38 77 77 — Télécopie : +33 4 92 38 77 65

Fusion d'autoradiographies et d'un volume IRM avec des transformations linéaires 2D et 3D

Résumé : Le développement des dernir̀es années des méthodes d'acquisition d'imagerie permettent d'avoir accès à une information anatomique (IRM, tomodensitomètre, ...), ou fonctionnelle (IRMf, TEMP, ...) *in vivo*. Malgré des progrès incessants, ces modalités n'ont pas une résolution ou un pouvoir de discrimination suffisamment puissant pour imager certains détails anatomiques ou fonctionnels, qui ne peuvent être révélés que par une imagerie *in vitro* (histologie, autoradiographie) éventuellement avec l'aide d'un produit de contraste ou de marquage adapté.

Ce travail est motivé par la comparaison des activations détectées par l'analyse de séries d'IRMf avec celles détectées dans des autoradiographies. Dans cette optique, le travail présenté dans ce rapport décrit la fusion des données autoradiographiques 2D avec une image IRM anatomique 3D. Dans un premier temps, un volume 3D cohérent en géométrie et en intensité est reconstruit à partir des données autoradiographiques. Ensuite ce volume est fusionné avec l'image IRM ce qui permet de corriger géométriquement la reconstruction afin de la rendre comparable à l'IRM.

En n'utilisant que des transformations (2D et 3D) globales simples (rigides et affines), nous montrons qu'il est possible d'aboutir à un volume autoradiographique reconstruit tout-à-fait comparable à l'image IRM *pre mortem*.

Mots-clés : Fusion, reconstruction, autoradiographie, IRM

1 Introduction

In the past years, the development of 3-D medical imaging devices has given access to the 3-D imaging of *in vivo* tissues, from an anatomical (MR, CT) or even functional point of view (fMRI, PET, SPECT). However, despite huge technological advances, the resolution of these images is still not sufficient to image anatomical or functional details, that can only be revealed by *in vitro* imaging (e.g. histology, autoradiography), eventually enhanced by staining [21].

The deep motivation of this work is the comparison of activations detected by fMRI series analysis to the ones that can be observed in autoradiographic (AR) images, and that can be considered as ground truth. Data are acquired on awake behaving animals (rhesus monkeys) in the laboratory of neuro- and psychophysiology of Professor G. Orban (Dept. of Neurosciences and Psychiatry, K.U. Leuven, Belgium).

In addition to the fMRI series, an anatomical MR image is also acquired against which fMRI images are registered. The aim of the presented work is to fuse the autoradiographic data with the pre-mortem anatomical MR image, so that comparison of detected activations (in term of location) will be straightforward.

The purpose of the fusion of a set of 2-D autoradiographies, or more generally a set of contiguous thin 2-D sections, with an MR volume of the same individual, is to find the most exact correspondance in the MR volume for each 2-D section. Fusion can be done following different strategies. Among these, the most intuitive consists in a twofold approach : first align the thin 2-D sections with respect to a chosen reference section, yielding a reconstructed 3-D volume; then co-register this 3-D volume to the MR volume.

Reconstruction of a 3-D volume from a stack of 2-D images (histological slices or autoradiographies) has already been largely studied. It is done by registering each two consecutive images in the stack to recover a geometrically coherent 3-D alignment of the 2-D slices. Main differences from images matching, as it is classically understood, are:

- slices to be registered are not images of the *same* object, but of *similar* objects (*i.e.* two consecutive sections) that can exhibit differences in shape and/or in intensity;
- non-coherent distortions may occur from one slice to the next.

The most common method is manual registration [6, 31]. Despite its simplicity, it has a number of drawbacks: it is not reproducible, it is user-dependent, and it is very time consuming that makes it not suitable for a large number of data.

Fiducial markers (e.g. by sticking needles in the material before slicing) can be tracked over the whole stack to recover the original geometry [7, 9, 10, 14]. However, since it is usually done by least squares minimization, a bias may appear if needles are not orthogonal to the cutting planes. Moreover, tracking can be awkward, particularly if needle holes collapse. Last, the needles may destroy part of the tissues of interest in the material.

More *classical* registration methods are also been investigated [36, 18]. Those methods can be divided in two classes: the geometrical ones that requires the segmentation of some features (points, lines, or even objects of interest), and the iconic ones that are based solely on the images' intensities.

Considering the geometrical methods, registration can first be achieved with global descriptors, e.g. centers of mass and principal axes. This has been proved of limited precision [34], but may be used as initialization [12, 11]. More precise features, *i.e.* contours [4, 12, 41], edges [15, 16], or points [26].

Because of the difficulty to design a completely automatic and reliable segmentation method, or to manually extract features of interest, iconic methods have also been investigated. They are based on the minimization (or maximization) of a given similarity measure of the images' intensities: cross-correlation in [12, 22] or mutual information in [17].

From our point of view, the work presented in [22] can be considered as an hybrid ICP[1]-like approach [2] between geometrical and iconic method: blocks can be considered as geometrical features while co-registration of blocks is achieved by minimization (or maximization) of a similarity measure. Hence we consider it as particularly suitable for the purpose of 3-D volume reconstruction.

Above is only addressed the problem of spatial alignment of the 2-D slices in order to reconstruct a geometrically coherent 3-D volume. It should be pointed that the problem of *alignment in intensity* have rarely been discussed. Indeed, 2-D autoradiographies may exhibit intensity inhomogeneities from one image to the other for several reasons (e.g. section's thickness). It can be easily compensated if appropriate standards (*microscales*) of known radioactivities are also imaged (and further scanned) on each piece of film [27]. If they are not present, alternative approaches have to be proposed.

The previously cited literature addresses only the problem of reconstruction of a 3-D volume from 2-D slices. It is of course of interest for many purposes but does not allow an easy comparison with *more classical* 3-D modalities (e.g. MRI, CT). The fusion of such histological or autoradiographic data with other 3-D data have been more rarely addressed. In this case, the specific transformations due to the acquisition protocol (e.g. cutting, manipulation, chemical treatment, etc.) have to be compensated. To our knowledge, histology has been co-registered with MRI [32, 33] and with PET [19]. In both cases, photographs are acquired during the cutting and used as an intermediate modality. A 3-D linear transformation is used to map the photographic volume onto the MR volume, while 2-D highly non-linear transformations compensate residual in-plane mis-alignements between the histological sections and the photographs.

In this paper, we address the fusion of 2-D autoradiographic slices with a 3-D anatomical MR image, when no intermediate modality, such as photographs, is available. In this case, it will be shown that it is an awkward task to retrieve, in the MR volume, the correspondance for each 2-D section. Moreover, we will demonstrate that it is possible to achieve a satisfactory correspondance by using only linear transformations.

The next section will present the data acquisition. In section 3, we describe the fusion methodology, that needs a first reconstruction of a 3-D volume with the 2-D autoradiogra-

---

[1] Iterative Closest Point.

phies, and the tools used for the different subtasks. The steps of the method are illustrated in section 4. Our method is then discussed in section 5.

2 Data

2.1 Acquisition protocol

2.1.1 MR image

Monkeys are trained for fMRI activations studies. During this period, several anatomical T1-weighted MR acquisitions are done, with anesthetized animals to avoid motion artifacts. Their average results in an MR image that has a size of $240 \times 256 \times 80$ with a voxel of 1 mm^3.

2.1.2 Autoradiographies

After fMRI studies have been performed, monkeys are trained for the autoradiographic study, for which a double-label deoxyglucose technique (DG) is used to distinguish between two activation paradigms (details can be found in [38, 8]). $[^3\text{H}]$deoxyglucose ($[^3\text{H}]$DG) is injected during the presentation of the first stimulus, then the second stimulus is presented and the $[^{14}\text{C}]$deoxyglucose ($[^{14}\text{C}]$DG) is injected.

After a short delay, the monkey is sacrificed (injection of sodium pentobarbital) and perfused transcardially (first with a saline solution to wash out the blood and second with a fixative solution). The brain is extracted from the skull, the hemisphere dedicated to our protocol is cut into two pieces and frozen as fast as possible (since the deoxyglucose marks the living cells and diffuses after death) each block lying on the cutting section so that it will still be plane after freezing.

Each block (posterior and anterior) is finally sectioned using a cryostat microtome (slice thickness of $40\,\mu$m), resulting in 818 slices for the posterior block and 887 slices for the anterior one. Sections are mounted on coverslips and dried. They are first exposed against ^{3}H sensitive films and second against ^{14}C sensitive films.

These films are subsequently manually scanned.

2.2 Acquisition analysis

The goal of this work is the fusion of the autoradiographic data with the MR image that serves as ground truth geometry. The above description of the acquisition may help us to understand the transformations that have occurred and that have to be compensated for.

- Perfusion yields a global shrinkage of the brain.
- Brain extraction causes a global non-rigid deformation (mostly bending).
- CSF goes away, resulting in local deformations (e.g. ventricles collapse).

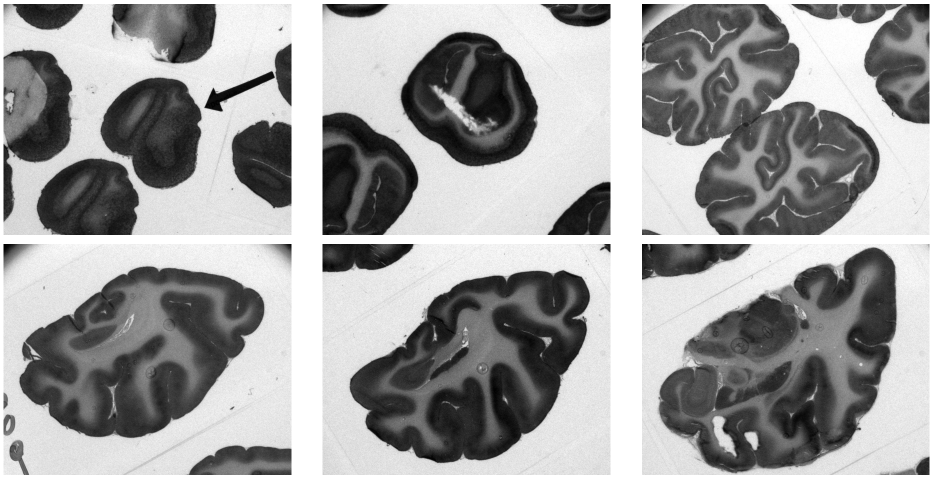

Figure 1: Some of the original autoradiographic images (out of 818) of the posterior block of the monkey's brain.

- In their position for freezing, the two blocks are submitted to biomechanical constraints (external pressure, gravity force, etc.) different than in living situation, this may yield non-rigid deformations.
- Freezing is also another cause of shrinkage.
- Sections cutting and positioning on films results in in-plane random transformations.

It should be pointed out that, while the first transformations are obviously three-dimensional and apply to the whole brain, the last item concerns 2-D independant transformations.

2.3 Preprocessing

2.3.1 Autoradiographies

Each brain section on the autoradiographic film out of the 818 has been scanned into a 1276×1024 image with a pixel of $40\,\mu\mathrm{m}^2$ and a slice thickness of $40\,\mu\mathrm{m}$ (see figure 1). These images are then subsampled by a factor 4 that results in 818 images of size 320×256 with a pixel of $160\,\mu\mathrm{m}^2$.

For economical reasons, each autoradiographic film may contain several brain sections, hence on one image several sections may be seen. With very simple operators (thresholding and mathematical morphology), we have extract the only section of interest in each image.

To facilitate this task, the scanning protocol was designed so that this particular section was centered in the image: this way the component to be extracted is the one containing the central point. Some images (e.g. the most posterior sections, that are very small) do not obey this protocol: in this case the sections of interest have been manually selected.

Nevertheless, it still failed for a few images where sections superimposed (e.g. last image of first row in figure 1): here the sections were manually segmented.

These processed sections are put into a stack resulting in a 3-D image of size $320 \times 256 \times 818$ with a voxel size of $0.16 \times 0.16 \times 0.04\,\mathrm{mm}^3$ (see top row of figure 4).

2.3.2 MR image

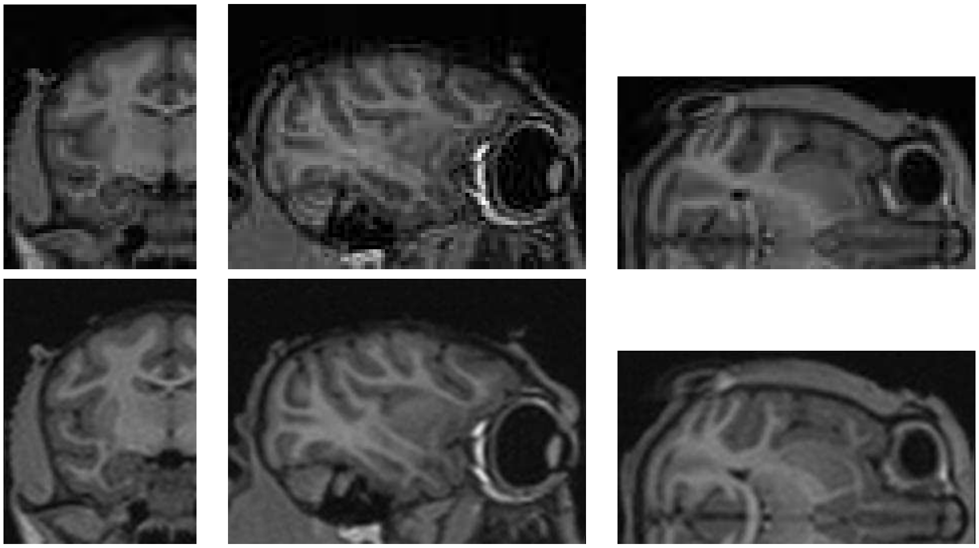

Figure 2: Top row: a region of interest (ROI) from the original MR image centered on the right hemisphere. Bottom row: this ROI supersampled by a factor 4 with cubic splines.

The original MR image has a size of $240 \times 256 \times 80$ with a voxel of 1 mm^3. From this image we first extract a sub-image of size $66 \times 89 \times 48$ that contains the right hemisphere of the brain.

We perform axis permutation on this sub-image so that it will be roughly in the same geometry than the stack of autoradiographies. Finally it has been supersampled by a factor 4 with cubic spline [35] to end up with an image of size $264 \times 192 \times 356$ with a voxel of 0.25 mm^3 (see figure 2).

3 Method

3.1 Framework

In this section, we first present the methodology of the fusion. We have chosen to separate this presentation from the tools we use, that will be presented in the next section, since we consider that alternative choices for these tools can be done.

The proposed fusion of a 3-D MR image with the autoradiographies consists in

1. a first reconstruction of an autoradiographic volume, coherent both in geometry and intensity, without the help of the MR image;
2. a *fusion loop*, that alternates between the reconstruction update of the autoradiographic volume with the help of the MR image and the 3-D registration of the autoradiographic volume against the MR image.

3.1.1 3-D reconstruction of an autoradiographic volume

The reconstruction of an 3-D autoradiographic volume from the 2-D autoradiographic slices S_i, $i = 1 \dots N$ is twofold.

Geometry consistency Following the scheme of [22], we realign the 2D slices to build a geometrically coherent volume.

Each couple of consecutive slices, S_i and S_{i+1} are rigidly co-registered, with the method described below (see section 3.2.1), yielding a 2-D transformation $T_{i \leftarrow i+1}$ (or equivalently $T_{i+1 \leftarrow i}$). A reference slice, of index ref_1, is chosen, and the 2-D transformations $T_{i \leftarrow ref_1}$ are computed by composition of the $T_{i \leftarrow i+1}$ or $T_{i+1 \leftarrow i}$ transformations.

All the resampled slices, $S_i \circ T_{i \leftarrow ref_1}$, can now be superposed to build a geometrically coherent 3-D volume. At this stage, a visual inspection is necessary, in order to detect some eventual mis-alignments that are due to a wrong co-registration between two consecutive slices (typically it concerns a small number of couples of slices, less than 2 %). To correct them, we change the default registration parameters and co-register again the mis-aligned couple of consecutive slices, until the found transformation is satisfactory.

Intensity consistency Because the overall illumination may change from one autoradiographic slice to another, we compensate for these changes with a dedicated histogram matching from slice to slice (see section 3.2.2), yielding an affine intensity transformation $f_{i \leftarrow i+1}$ (or equivalently $f_{i+1 \leftarrow i}$) between two consecutive slices. A reference slice, of index ref_2, is chosen, and the intensity transformations $f_{ref_2 \leftarrow i}$ are computed by composition of the $f_{i \leftarrow i+1}$ or $f_{i+1 \leftarrow i}$ intensity transformations.

To summarize, the 3-D reconstruction of an autoradiographic volume, coherent in geometry and in intensity, is achieved by the superposition of the resampled slices $f_{ref_2 \leftarrow i} \circ S_i \circ T_{i \leftarrow ref_1}$.

3.1.2 Initial 3-D registration MRI / autoradiographic volume

The reconstructed autoradiographic volume AV is coregistered with the MR volume (see section 3.2.1), providing an initial solution to our fusion problem. At this point we only consider 3-D rigid transformation.

3.1.3 Fusion loops

This loop aims to fuse the 2-D autoradiographic slices with the 3-D MR image, given a first 3-D reconstruction of the autoradiographic volume, $AV^{(0)}$, and the initial 3-D transformation $T_{MR \leftarrow AV^{(0)}}$ (as obtained above). Each iteration k of the loop is divided into four steps.

1. This first step is twofold;
   (a) Resampling of the MR volume into the geometry of $AV^{(k)}$ yielding the volume $\widetilde{MR}^{(k)} = MR \circ T_{MR \leftarrow AV^{(k)}}$. This allows to extract MR slices, $\widetilde{MR}_i^{(k)}$, $i = 1 \ldots N$, that correspond to autoradiographic slices.
   (b) 2-D registrations of each autoradiographic slice $AV_i^{(k)}$ against the corresponding resampled MR slice, resulting in N 2-D independent transformations $T_{AV_i^{(k)} \leftarrow \widetilde{MR}_i^{(k)}}$ (see section 3.2.1).
2. Filtering of the 2-D independent transformations $T_{AV_i^{(k)} \leftarrow \widetilde{MR}_i^{(k)}}$, yielding the 2-D correlated transformations $\hat{T}_{AV_i^{(k)} \leftarrow \widetilde{MR}_i^{(k)}}$ (see section 3.2.3).
3. Building of a new autoradiographic $AV^{(k+1)}$ volume by superposing the slices $AV_i^{(k)} \circ \hat{T}_{AV_i^{(k)} \leftarrow \widetilde{MR}_i^{(k)}}$.
4. 3-D registration of the autoradiographic volume $AV^{(k+1)}$ against the 3-D MR image, yielding a 3-D transformation $T_{MR \leftarrow AV^{(k+1)}}$ (see section 3.2.1).

This loop, that alternates between the reconstruction update of the autoradiographic volume and the 3-D registration of the autoradiographic volume against the MR image, is summarized in figure 3.

We only use global parametric transformations in this loop, *i.e.* rigid transformations, similarities, or affine transformations. More precisely, our choices for the transformation classes are given in table 2.

3.2 Tools

3.2.1 2-D and 3-D Registration

To register 2 images, that can be either two 2-D autoradiographies or the 3-D autoradiographic reconstructed volume and the 3-D MR volume, any registration method can in

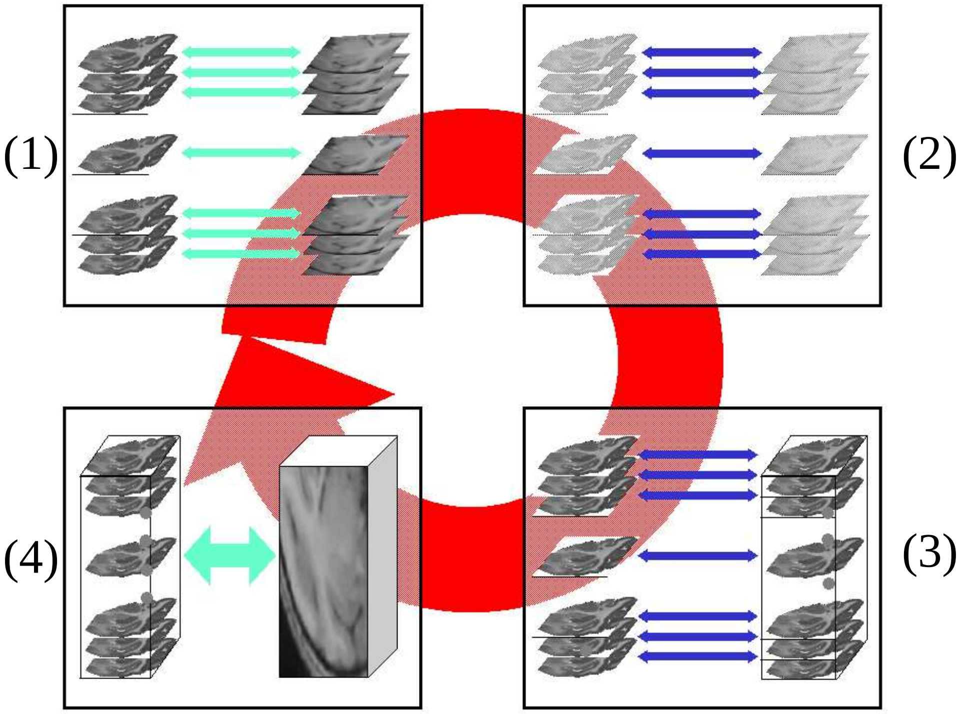

Figure 3: Fusion loop: (1) independent 2-D registrations for each pair autoradiographic slice / MR resampled slice; (2) filtering of the 2-D transformations; (3) reconstruction of an autoradiographic volume; (4) 3-D registration autoradiographic volume / MRI.

principle be used [36, 18]. We will neither discuss nor justify the method we choose, namely block matching, that is particularly suited for 3-D reconstruction since it has already been described and discussed in [22]. It can be considered as an hybrid ICP[2]-like approach [2] between geometrical and iconic method: blocks can be considered as geometrical features while co-registration of blocks is achieved by minimization (or maximization) of a similarity measure. We will only recall here its main features.

This algorithm takes as input a reference image I and a floating image J, and aims to estimate a transformation T such as $J \circ T$ can be superimposed on I. It is done through an iterative scheme: at each stage, correspondences are computed thanks to a block matching algorithm, and a transformation δT is estimated with these correspondences that allows to update the searched transformation T.

---

[2] Iterative Closest Point.

Block matching In this paragraph, we will describe the block matching strategy. The transformation T is computed iteratively. Let us denote its estimation at step k by T_k (with $T_0 = \text{Identity}$).

A block $B(x, y)$ in image I is defined as the sub-image of I with upper left corner (x, y) and dimensions $d_x \times d_y$. For each block, we can compute its average value $\overline{B}(x, y)$ and its standard deviation $\sigma(x, y)$. We define the set $\mathcal{B}_{a,b}$ of blocks by

$$\mathcal{B}_{s_x,s_y} = \{B(x, y) \subset I \text{ such that } x = as_x, y = bs_y \text{ with } a, b \in \mathbb{N}\}$$

It comes out that $\mathcal{B}_{1,1}$ contains all the possible blocks of size $d_x \times d_y$ included in I, while $\mathcal{B}_{s_x,s_y}$ with $s_x > 1$ or $s_y > 1$ contains only a subset of them.

Considering large values of s_x and s_y decreases the number of considered blocks in I, and thus decreases the computational cost, but important features of I may also be missed. We choose then not too large s_x and s_y, but we remove from the set $\mathcal{B}_{s_x,s_y}$ the blocks with the lowest standard deviation value[3]. We thus only keep a percentage p of blocks of $\mathcal{B}_{s_x,s_y}$, that results in a final set of blocks $\mathcal{D}_{s_x,s_y}$ of I.

Once the blocks to be considered in I are defined, we compute, for each of them its best correspondence in $J \circ T_k$ (*i.e.* J resampled with T_k). To achieve that, we look for the block $B'(x', y')$ of upper left corner (x', y') and size $d_x \times d_y$ in $J \circ T_k$ that optimizes a similarity measure S

$$B'(x', y') = \arg \max_{B'(u,v) \subset J \circ T_k} S(B(x, y), B'(u, v))$$

Still for practical reasons, the search for $B'(x', y')$ is limited to a region of interest centered in (x, y).

$$B'(x', y') = \arg \max_{B'(u,v) \subset J \circ T_k, (u,v) \in [x-r_x, x+r_x] \times [y-r_y, y+r_y]} S(B(x, y), B'(u, v))$$

The choice of the similarity measure should depend on the expected relationship between the block intensities. Considering that a block may contains up to two (and rarely three) different tissues, an affine relationship seems reasonable. Hence, we choose the correlation coefficient as the similarity measure [28].

$$S(B(x, y), B'(u, v)) = \frac{1}{d_x d_y} \frac{1}{\sigma(x, y)\sigma'(u, v)} \sum_{a=0 \ldots d_x-1} \sum_{b=0 \ldots d_y-1} \left[I(x + a, y + b) - \overline{B}(x, y)\right] \left[(J \circ T_k)(u + a, v + b) - \overline{B}'(u, v)\right]$$

where $\overline{B}'(u, v)$ and $\sigma'(u, v)$ are the average value and the standard deviation of the intensities of block $B'(u, v)$.

---

[3] Blocks with low standard deviation are likely to contain only one type of tissue, yielding not reliable correspondences, while the ones with the highest standard deviation are more likely to contain different types of tissue, and yield more reliable correspondences.

	d_x	d_y	d_z	s_x	s_y	s_z	r_x	r_y	r_z	p	l
2-D	4	4	-	3	3	-	3	3	-	80 %	6
3-D	4	4	4	3	3	3	3	3	3	100 %	3

Table 1: Typical values of the parameters for both the 2-D and the 3-D registration algorithms

From each pair of corresponding blocks, $B(x,y)$ and $B'(x',y')$, we deduce a pair of corresponding points, $C(x,y)$ and $C'(x',y')$, being respectively the centers of blocks $B(x,y)$ and $B'(x',y')$.

The optimal transformation δT_k between the images I and $J \circ T_k$ would be the one minimizing the residuals $\|C(x,y) - \delta T(C'(x',y'))\|^2$ in a least squares sense. To reject outliers, a robust estimation with a weighted Least Trimmed Squares (LTS) is prefered [30]. M-estimators could have be chosen as well [40].

After this estimation, the value of the transformation T is updated with $T_{k+1} = \delta T_k \circ T_k$. This iterative procedure stops as soon as no significant change occurs in the transformation evaluation.

Multiscale implementation Large transformations can only be captured by using both large regions of search (large values of r_x and r_y), and large blocks (in order to avoid local minima in the similarity measure), and thus at a high computational cost, while smaller transformations can be captured with smaller blocks and smaller regions of search.

Hence, to be able to capture even the large displacements, we have implemented the block matching within a multiscale strategy.

Each image is represented by a pyramid of l levels where each level is the image resampled by dividing the image dimensions by a factor 2. The registration is done at each level, while the initial transformation comes from the previous level.

3.2.2 Intensity compensation

Consider two discrete histograms or equivalently two discrete probability density functions (PDF) $p(x_i)$ and $q(y_j)$, with $x_i, y_j \in \mathbb{Z}$, the aim of this section is to estimate an intensity transformation f such that the distribution p is *similar* to $q \circ f$. This problem is known as histogram matching.

Classically, this can be solved via histogram equalization. This last operation consists in transforming one histogram into a flat histogram [3]. Thus, matching two histograms can be achieved by (implicitly) using this flat histogram as intermediary [13]. This approach is not robust at all, as it depends highly on the extremal values of the intensity histogram. Moreover, we want to estimate global parametric intensity functions (e.g. affine), that makes the above approach not suitable.

Thus, our problem is as follows: given an intensity transformation function class $\mathcal{F}$, find the *best* function $\hat{f} \in \mathcal{F}$ such that $y = f(x)$, *i.e.* solve

$$\hat{f} = \arg \min_{f \in \mathcal{F}} S(p(x_i), q(y_j), f)$$

where S is some similarity measure of histograms.

Because of the discretisation (binning, etc), it is not possible to directly compare the discrete pdf $p(x_i)$ to $q \circ f(x_i)$. Instead, we will first estimate the continuous pdf corresponding to q, transform it with function f, and build from this transformed continuous pdf the discrete one corresponding to the x_i bins.

There exists many ways to estimate a continuous pdf from discrete samples or from an histogram. We choose the most common one, *i.e.* the so-called Akaike-Parzen-Rosenblatt windowing technique [1, 24, 29]. The continuous pdf $Q_s(x)$ estimated from $q(y_j)$ will then be

$$Q_s(y) = \sum_j p(y_j) K_s(y - y_j)$$

where $s > 0$ is a smoothing factor, K is a non negative absolutely integrable function (called the kernel). Our particular choice for the kernel function is the Gaussian, and the smoothing factor is then the standard deviation σ.

Building now the discrete pdf $q \circ f(x_i)$ is now straightforward: for each bin x_i, we only have to integrate $Q_s(y)$ in the interval $[x_i^{min}, x_i^{max}]$ that defines the bin x_i.

$$(q \circ f)_s(x_i) = \sum_j q(y_j) \int_{f(x_i^{min}) - y_j}^{f(x_i^{max}) - y_j} K_s(u) du$$

Because of the *smoothing* effect of the kernel, we will not compare $(q \circ f)_s(x_i)$ directly against $p(x_i)$ but against $p_s(x_i)$ with

$$p_s(x_j) = \sum_i p(x_i) \int_{x_j^{min} - x_i}^{x_j^{max} - x_i} K_s(x) dx$$

This formulation may introduce some asymmetry in the criteria to minimize. To overcome this, it can be changed into

$$\hat{f} = \arg \min_{f \in \mathcal{F}} \left(S\left(p_s(x_i), (q \circ f)_s(x_i)\right) + S\left((p \circ f^{-1})_s(y_j), q_s(y_j)\right) \right)$$

when f is easily invertible.

Our practical choice for this application is to use affine function f, and minimization is done with a classical Powell-Brent procedure. We implemented several similarity measures, among others the sum of squared differences and the maximum of the likelihood, that both yield visually good results.

3.2.3 Filtering of transformations

The problem is as follows: we got a set of transformations $T(i)$ belonging to transformation class $\mathcal{T}$ and we want to estimate a filtered transformation $\hat{T}(i) \in \mathcal{T}$ such that

$$\hat{T}(i) = \arg \min_{T \in \mathcal{T}} \sum_j g(i-j) \mathrm{dist} \left(T(j), T \right)^2$$

where $g()$ is some low pass filter, *e.g.* a Gaussian function, and dist() represents a distance for $\mathcal{T}$.

Such a computation is not straightforward [25] but can be achieved with the Fréchet expectation. Since this expectation can be approximated by the standard expectation near the origin (*i.e.* the identity), we use this property to compute the Fréchet expectation with an iterative procedure that then needs a first estimate of $\hat{T}(i)$, *e.g.* $\hat{T}_{(0)}(i) = T(i)$:

$$\hat{T}_{(k+1)}(i) = \hat{T}_{(k)}(i) \circ \left[\sum_j g(i-j) \left(\hat{T}_{(k)}^{(-1)}(i) \circ T(j) \right) \right]$$

It stops when $\sum_j g(i-j) \left(\hat{T}_{(k)}^{(-1)}(i) \circ T(j) \right)$ is close enough to the identity.

We now have to precise how to compute a weighted sum of transformations $\sum_j w_j T(j)$ *within* a given class of transformation $\mathcal{T}$.

- It is straightforward for affine transformations that can be represented by matrices $T(j) = [t_{u,v}(j)]$ in homogeneous coordinates since the weighted sum can be achieved on the matrices' elements.

$$\hat{T}(i) = [\hat{t}_{u,v}(i)] \quad \text{with} \quad \hat{t}_{u,v}(i) = \sum_j w_j t_{u,v}(j)$$

- To deal with rigid transformations, we represent them by their rotation and translation vectors: $T(j) = (\mathbf{v}(j), \mathbf{t}(j))$. We have then

$$\hat{T}(i) = (\hat{\mathbf{v}}(i), \hat{\mathbf{t}}(i)) \quad \text{with} \quad \hat{\mathbf{v}}(i) = \sum_j w_j \mathbf{v}(j) \quad \text{and} \quad \hat{\mathbf{t}}(i) = \sum_j w_j \mathbf{t}(j)$$

4 Results

4.1 Reconstruction of the autoradiographic volume

A first reconstruction of the autoradiographic volume has been performed by registering each couple of consecutive sections with the 2-D block matching algorithm (typical values of parameters are given in table 1). The composition of computed transformations permits to register all sections against a reference section (taken at the middle of the stack).

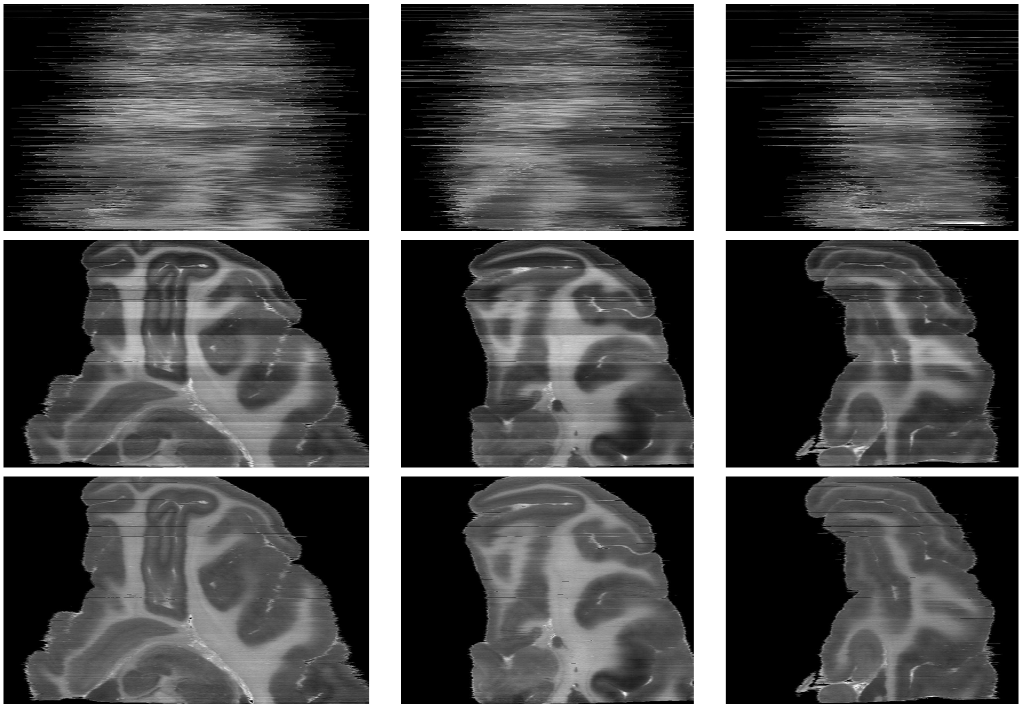

Figure 4: From left to right: one axial and two sagittal slices of the reconstructed autoradiographic volume of the posterior block. First row: before any correction. Second row: after geometric alignment of the slices, and before intensity correction. Third row: after intensity correction.

Visual inspection of the reconstructed volume allows to detect eventual remaining registration errors that are subsequently corrected by changing registration parameters. This control step is repeated until the results is satisfactory, *i.e.* until the reconstructed volume seems geometrically consistent. First row of figure 4 shows the stack of autoradiographies to be compared to the obtained reconstruction (second row of same figure).

Intensity consistency is also obtained by performing histogram matching (see section 3.2.2) for each couple of consecutive sections. Please note that this computation is independent from the above geometrical registration. Several criteria (sum of squared differences (SSD), correlation, maximum of likelihood (ML)) together with several kernel's smoothing factor ($\sigma \in \{3, 5, 8, 12\}$) have been tested, and one among the visually satisfactory results (e.g. SSD and ML with $\sigma = 5$) has been picked for the further steps. Last row of figure 4 depicts the final reconstruction.

4.2 Initial registration with MRI

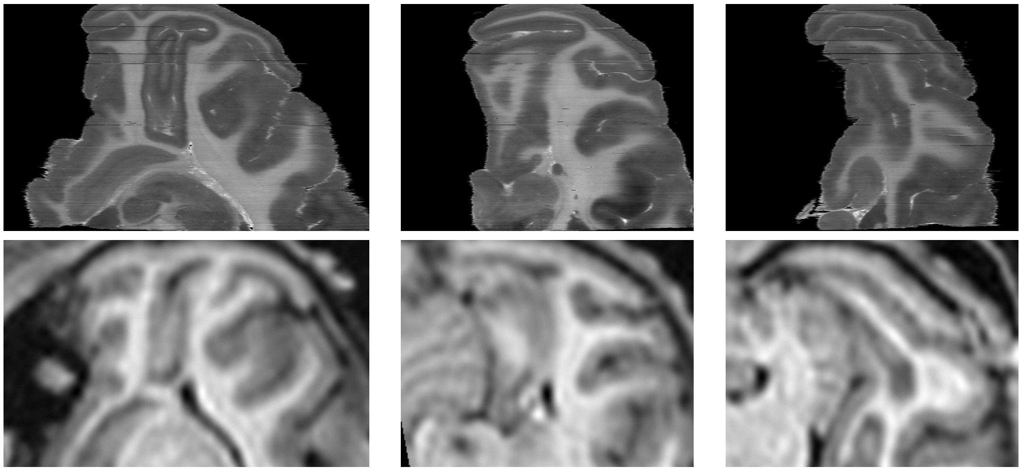

Figure 5: Top row: same as last row of figure 4. Bottom row: corresponding slices of the resampled MR volume after 3-D rigid registration.

After reconstruction of the autoradiographic volume, it can be registered (here rigidly) against the MR sub-volume of interest (the corresponding hemisphere). Top row of Figure 5 shows cross-sections of the reconstructed AR volume while the bottom row shows the corresponding cross-sections of the resampled MR volume after registration. Both volumes are roughly similar, but large differences can be seen especially in posterior areas.

4.3 Fusion loops

According that the AR volume has already been rigidly registered against the MR volume, the fusion loops consist in iterating these three successive steps:

1. 2-D independent registrations of each AR section against the corresponding slice of the resampled MR volume,
2. filtering of the 2-D transformations,
3. reconstruction of a new 3-D AR volume,
4. and 3-D registration of the newly reconstructed AR volume against the MR volume.

	2-D registrations $T_{AV_i^{(k)} \leftarrow \widetilde{MR}_i^{(k)}}$	2-D transformations filtering $\sigma_{(k)}$	3-D registration $T_{MR \leftarrow AV^{(k+1)}}$
Loop # 1	rigid	10	affine
Loop # 2	rigid	8	affine
Loop # 3	affine	10	affine

Table 2: Fusion loop, choice of the parameters: transformations classes and 2-D transformations filtering.

The different transformation classes that have been considered through the fusion loops can be found in table 2. We stop after the fourth registration between MR and AR volumes since no changes occur at this step.

Intermediary results for loop # 1 are given in figure 6; figure 7 shows the final alignement of the histological slices with respect to the MR volume.

Figure 8 highlights the gains due to the proposed fusion methodology: top, middle, and bottom rows show cross-sections of respectively the original MR sub-volume of interest (the right hemisphere), the first reconstructed and resampled AR volume after rigid registration, and the final reconstructed and resampled AR volume after affine registration. Contours [20] extracted from the presented MR cross-sections are superimposed on the AR cross-sections in Figure 9.

Gains along the fusion process can be seen in figure 10 that presents the differences between any two successive autoradiographic volumes (registered against the MR image). Displacements are large after loop #1, and become smaller between loop #2 and loop #3.

This may suggests that further improvements could be reached by keeping on smoothly increasing the number of degrees of freedom of the transformations.

We have also fused the anterior part of the same monkey's brain (see figure 11) to the MR volume. As we did observe only minor changes between loops #1 and #2, we did not go into the third loop. Indeed, the so-called *banana problem* (see section 5) was less present in this case.

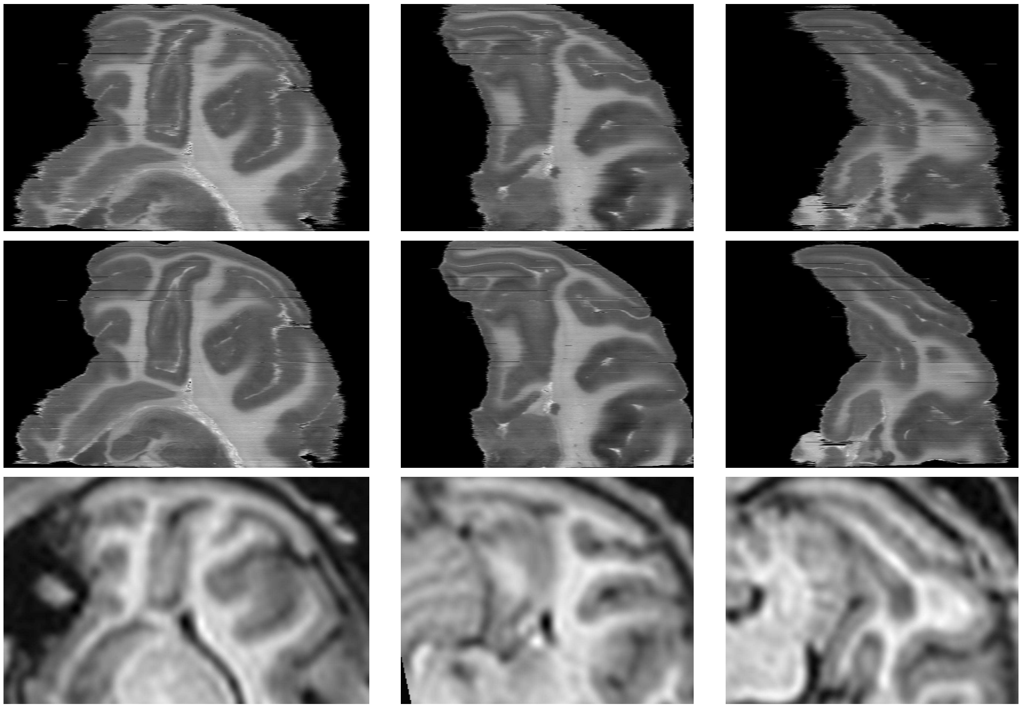

Figure 6: Fusion loop # 1. From left to right: one axial and two sagittal slices. First row: autoradiographic volume after the independent 2-D slice registration. Second row: autoradiographic volume after smoothing of the 2-D transformation. Third row: MR image resampled after affine registration against the above reconstructed AR volume. The effect of this first loop can be appreciate by comparing the middle row to the first row of figure 5.

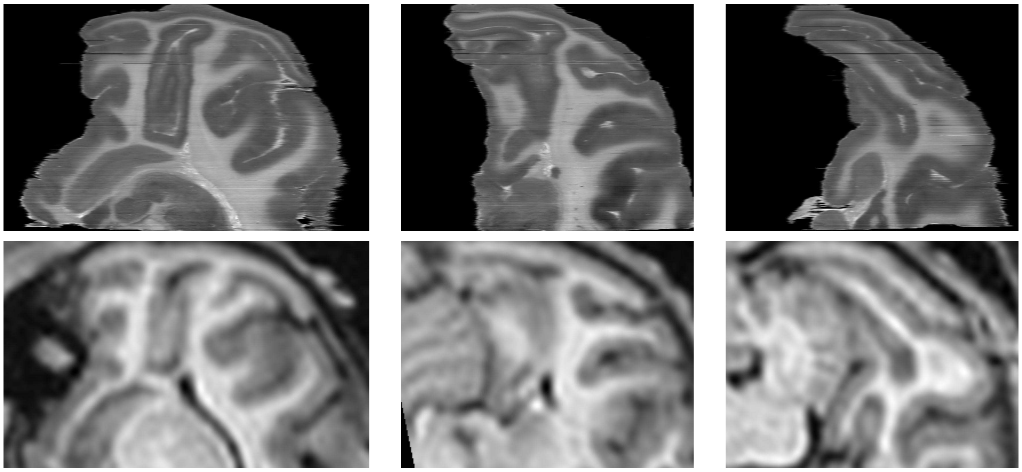

Figure 7: Fusion loop # 3. From left to right: one axial and two sagittal slices. First row: autoradiographic volume after smoothing of the 2-D transformation. Second row: MR image resampled after affine registration against the above reconstructed AR volume.

4.4 Expert based visual inspection

The deep motivation of the presented work will be the comparison of activations detected from autoradiographies to the ones detected in fMRI series study. More precisely, we are interested in the visual cortex [39, 38]. It comes out that our work may serve our purpose if the sulci involved in the visual cortex are well registered.

This have been visually checked by experts with two different tools. On one hand, the two volumes in the same geometry (here the one of the MR) can be seen in two synchronized 3-D viewers: both of them always display the same cross-sections (axial, sagittal and coronal) as well as a cursor at the same place (see the two snapshots at the left of figure 11). On the other hand, the two volumes can be visually superimposed, different color maps being eventually applied (see the right snapshot of figure 11) [5].

Both tools allow navigation in the fused 3-D volumes which permits to check the correctness of the fusion. At the level of the visual cortex, the correspondence is very accurate, as well as for most of the brain. Some small mismatch errors can be seen at the medial side of the caudate nucleus (due to ventricles collapse).

5 Discussion

5.1 Reconstruction

This step is made of two parts, a geometry-based and an intensity-based reconstruction.

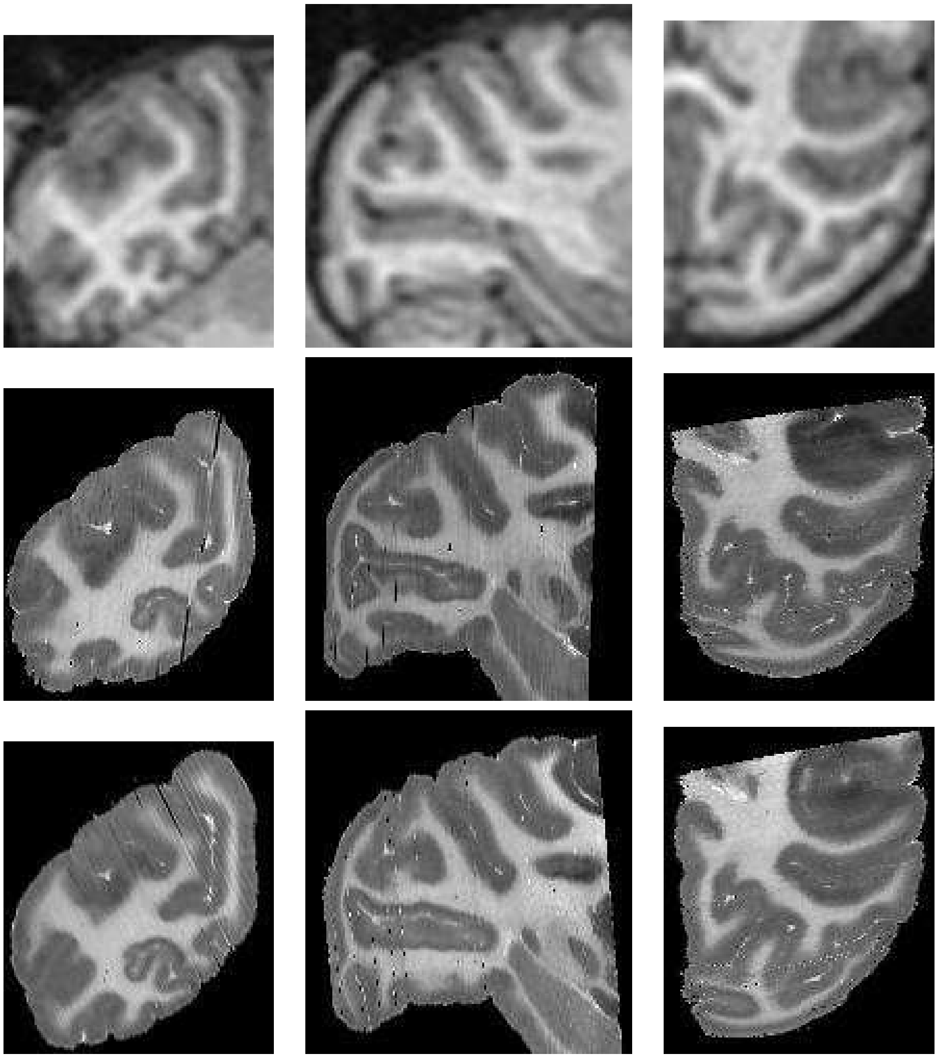

Figure 8: From left to right: coronal, sagittal, and axial slices in the acquisition geometry of the MR image. Top row: the MR image (resampled with cubic splines, see figure 2). Middle row: the 3 same slices of the first reconstructed autoradiographic volume (before any fusion loop) rigidly registered against the MR image. Bottom row: the 3 same slices of the last reconstructed autoradiographic volume (after all fusion loops) registered against the MR image.

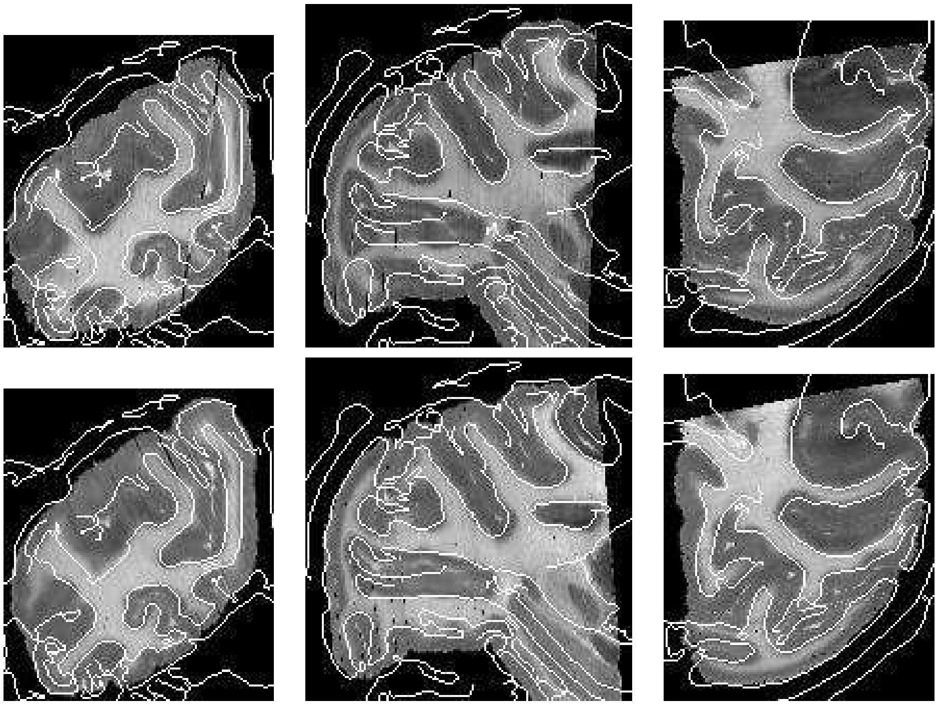

Figure 9: The contours extracted from the MR image (first row of figure 8) superimposed on the corresponding slices of two bottom rows from the same figure.

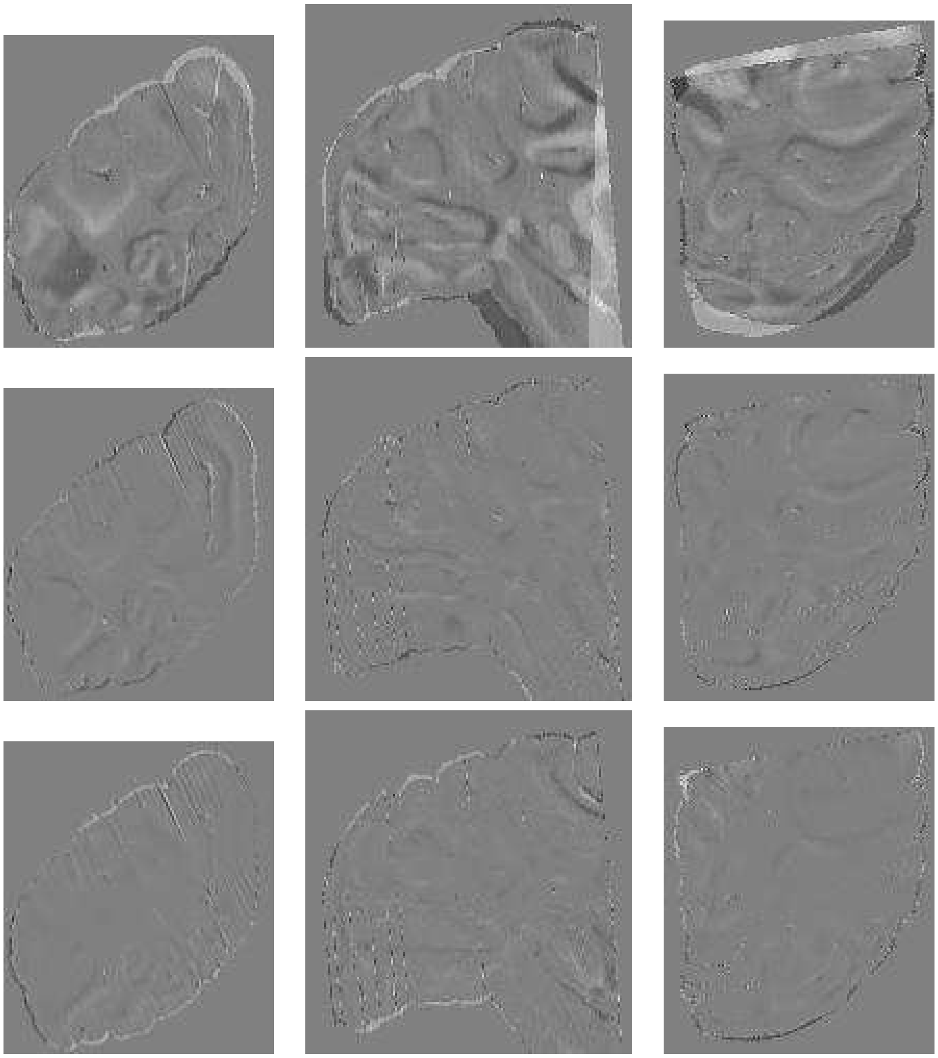

Figure 10: Difference images bewteen the successive autoradiographic volumes (AV) registered against the MR image. First row: AV after loop #1 minus first reconstructed AV. Second row: AV after loop #2 minus AV after loop #1. Third row: AV after loop #3 minus AV after loop #2.

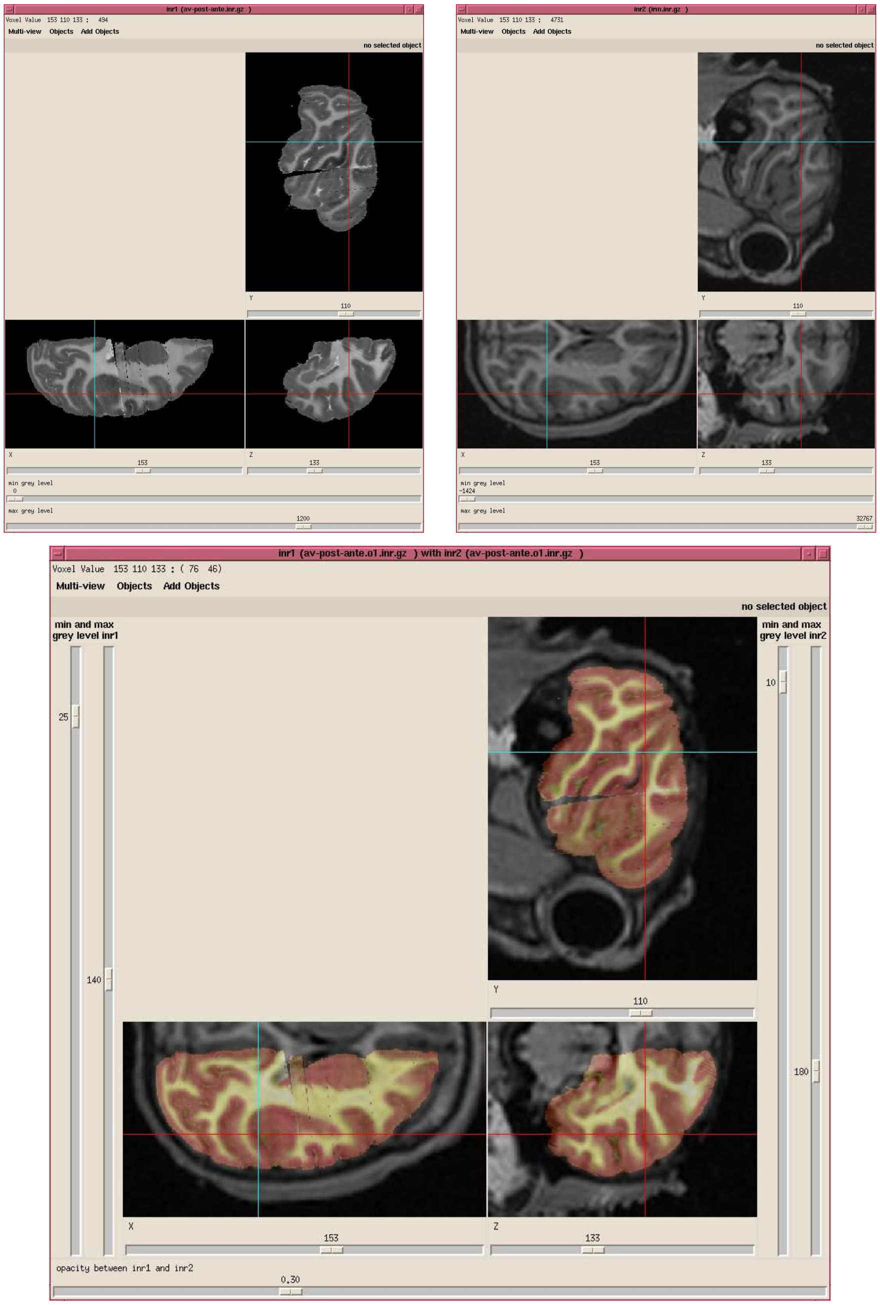

Figure 11: Fused images can be presented in two different viewers, but with synchronized cursors, *i.e.* at the same position in both viewers, (two images at the top), or in a single viewer with different color tables (image at the bottom).

Concerning the geometrical reconstruction, a visual inspection (and eventually correction) is necessary in case of mismatch between two consecutive sections. It should be pointed out that *mismatch* does not mean *poor accuracy*. Indeed, it has been proven that the block matching algorithm gives accurate results [22, 23] given that initial conditions are in the convergence basin. If not, *i.e.* in case of failure, there is a huge discrepancy between the obtained transformation and the expected one so that the failure can very easily be seen. This is emphasized by the the reconstruction obtained by transformations' composition: two mismatched consecutive sections will separate two geometrically consistent 3-D sub-volumes. We correct these errors y changing the registration parameters: this modifies the shape of the convergence basin so that it will contain the initial position. Another solution could have been to change the initial transformation parameters (initial transformation is set to identity) but this has not be explored.

Visual inspection of the intensity-based reconstruction is facilitated by the same remark as above. A single error (a mismatch in matching the histogram of two consecutive sections) results, after reconstruction, in a separation between two intensity-consistent 3-D sub-volumes.

It can be questioned whether this intensity-based reconstruction is necessary or not (independently of esthetic considerations). The answer is clearly yes without any additional assumption on the autoradiographies' acquisition. Indeed, the 3-D reconstructed AR volume will be registered against the MR volume. To do this, 3-D sub-images (blocks) of the AR volume will be compared to 3-D blocks of the MR volume with the correlation coefficient that assumes an affine relationship between intensities and thus needs each of both blocks to be consistent in intensity. Obviously, it is not possible to find the right correspondence for a block that is not so. Since our implementation of block matching is robust (can reject outliers), it may still compute the expected 3-D transformation if there are not *too many* corrupted blocks, e.g. if there are only very few intensity *jumps* in the AR volume. Without such additional assumption, it comes out that intensity-based reconstruction is also necessary.

Note that reconstruction as addressed in this section refers to the alignment of the 2-D sections only. We discuss in the next section the intrinsic problem of the correctness of such a direct reconstruction, highlighted when fusing the resulting 3-D volume with an MR volume.

5.2 Fusion

Fusion of a set of 2-D autoradiographies, or more generally a set of contiguous thin 2-D sections, with an MR volume of the same individual, can be done following a twofold approach: first align the thin 2-D sections with respect to a chosen reference section, yielding a reconstructed 3-D volume; then co-register this 3-D volume to the MR volume.

Obviously, as a result of such a fusion, one expects to have found the most exact correspondance in the MR volume for each 2-D section. Moreover, the fusion purpose is to build a transformation that makes the sections to slide on each other, thus ensuring that they stay parallel to each other, somehow preserving their integrity.

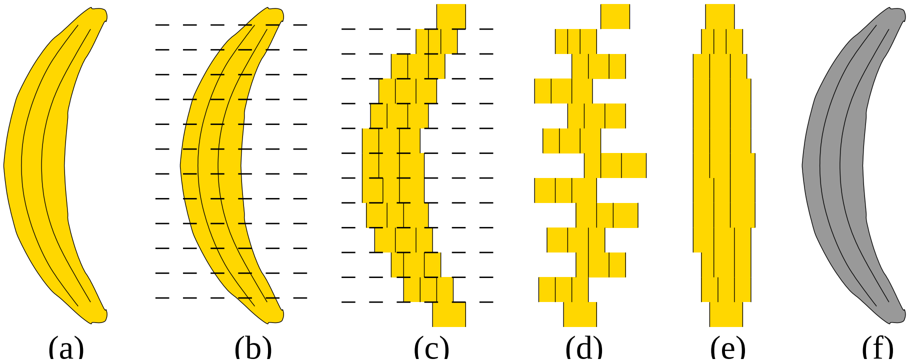

Figure 12: The banana's problem: the 3-D reconstruction of a 3-D curved object is not easy. a) Take a 3-D curved object (e.g. a banana); b) cut it into slices; c) digitize the slices; d) mix the digitized slices; e) the 3-D reconstruction results in a cylindrical banana. f) Using a shape prior (e.g. MRI) may help to reconstructed the curved banana.

But one of the main difficulties of the reconstruction of a 3-D volume from 2-D sections (either histological or autoradiographic) comes from what we call the banana's problem (illustrated in figure 12): a 3-D curved object can not be reconstructed from cross-sections without any additional information.

The acquisition protocol can be designed so that it includes such additional information provided by some fiducials. One way is to stick needles in the material before slicing, as it will provide correspondences which then drive the geometry-based reconstruction [7, 9, 10, 14]. However, reconstruction can be awkward, particularly if needles are not orthogonal to the cutting plane or if needle holes collapse. Another way is to take photographs of the unstained surface of the material during the slicing process, incuding a reference system fixed on the cryomicrotome [32, 33, 19]. Alignment of the photographs using the reference system will then provide a photographical 3-D volume with the real geometry of the object under study, e.g. the brain after extraction from the skull but before slicing and staining. Thus further reconstruction of the 2-D histological sections into a geometrically consistent 3-D volume can be made by independant registrations of the 2-D sections with the corresponding previously aligned photographs.

When such *a priori* additional information about the real geometry of the object under study is available, the banana's problem obviously doesn't appear. Nevertheless, it is not always possible, for practical reasons, to dispose of such information. In that case, the only information about the geometry of the brain before slicing is given by the anatomical MR volume.

Here, one could have thought that a direct and strict twofold approach, namely reconstruction of a 3-D volume by alignment of the 2-D sections followed by the registration of this volume with the anatomical MR volume, would directly provide a satisfactory result.

This implicitly assumes that either the computed 2-D transformations will compensate the random in-plane transformations due to the acquisition procedure, which is not realistic for curved objects, or that further 3-D elastic registration may compensate for the residual distortions.

However, existing elastic transformations implemented in such algorithms are obviously not adapted. First they consider in a similar manner the 3 directions of space. In our particular problem, one direction (the one orthogonal to the cutting plane) plays clearly a different role. Moreover, from a methodological point of view, it simply ignores the acquisition reality (see section 2.2). Precisely, transformations that have occurred during the acquisition are clearly of different types, that is: 3-D, rather smooth and applied to the whole brain, or 2-D and independant from section to section.

The proposed fusion methodology mimics the acquisition procedure by considering both a stack of 2-D transformations (that correspond to the displacements of the AR sections) and a 3-D transformation corresponding to the registration against the MR volume.

More precisely, after an initial reconstruction of the 2-D sections, we alternate between the correction of this reconstructed AR volume (by recomputing the 2-D transformations) and a 3-D registration with the MR volume. By doing this, we expect to better estimate the random in-plane transformations due to the acquisition procedure, together with the relative position of the reconstructed volume with respect to the MR volume. The choice of the transformation search spaces during these fusion loops, namely starting with strongly constrained ones (i.e. rigid) and slightly relaxing (ending with affine ones both in 2-D and 3-D), is made such as to preserve integrity (e.g. constant slice thickness) of the AR sections. In other words, we don't allow the AR sections to be strongly deformed before their corresponding MR slices have been localized for a given transformation search space.

It should be pointed out that the obtained result is much more than satisfactory, although it only involves a stack of 2-D and 3-D linear transformations.

Figure 13 illustrates the banana's problem with our data. It shows (in blue) the vertical central line of the first 3-D reconstruction of the AR volume (last row of figure 4) that could be considered as the symmetry axis of the cylindrical reconstructed object, and the deformation of this line (in red) after the fusion: a curvature appears clearly.

Figure 14 compares the result of the fusion using our approach and a straight twofold approach. It shows (middle row) a direct registration using affine transforms of the reconstructed AR volume with the MR volume, compared to the final result using fusion loops (bottom row). This shows that a direct 3-D affine transformation is obviously not sufficient to model the deformation between the initial AR reconstructed volume and the MR volume. More precisely, it can be seen on the middle row of Figure 14 that the anterior part of the AR volume is quite well registered, while large deformations are still to be recovered for the posterior part. It suggests that a further 3-D elastic registration (usually initialized by a rigid or affine transformation) would result in inhomogeneous deformations of the AR slices along the antero-posterior axis. Thus we suspect that doing so would alter the integrity of the AR slices and finally not give the most exact correspondance in the MR volume for each 2-D AR section.

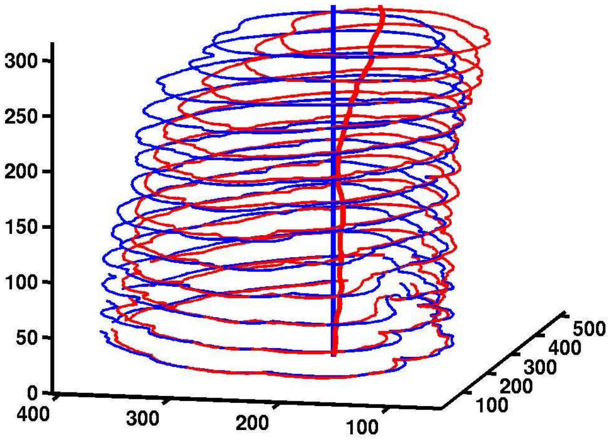

Figure 13: The banana's problem: illustration with the posterior block. In blue, some outer 2-D contours and the central line of the image after the first 3-D reconstruction (last row of figure 4). In red, the same after applying the fusion loops' transformations (middle row of figure 7).

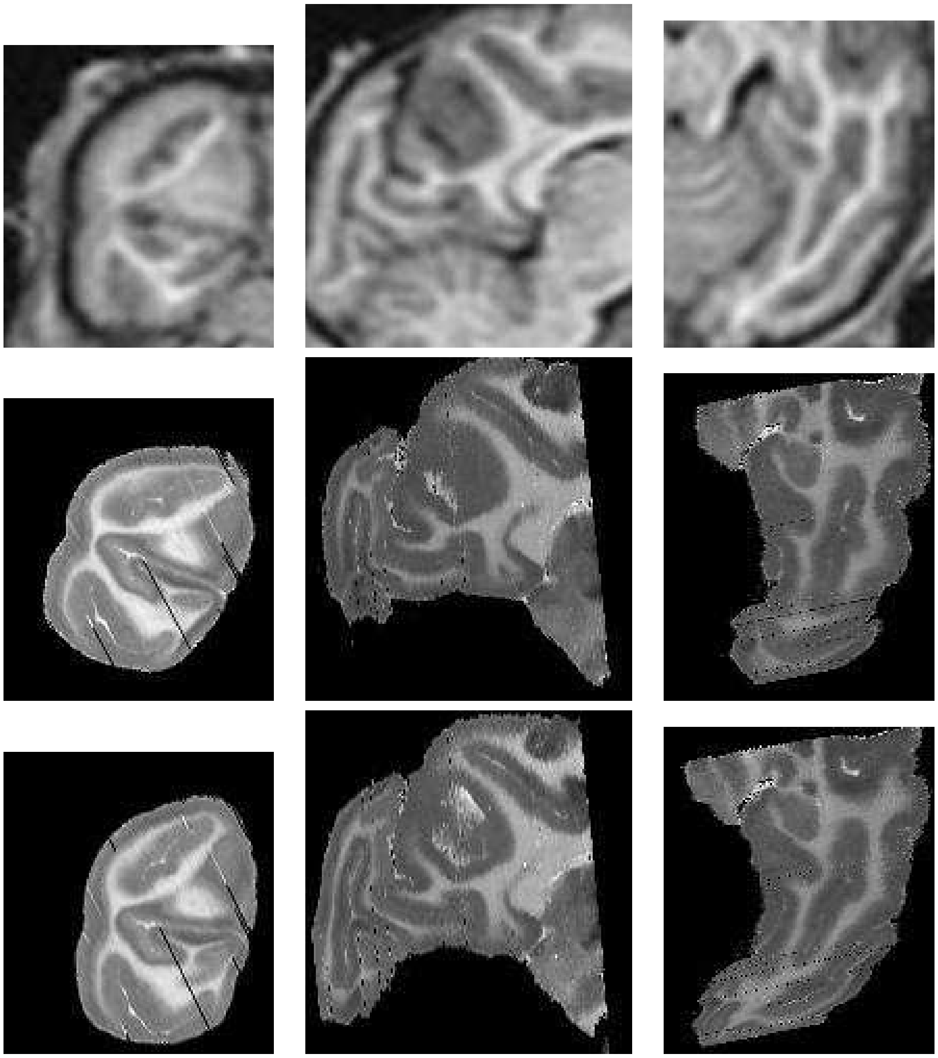

Figure 14: From left to right: coronal, sagittal, and axial slices in the acquisition geometry of the MR image. Top row: the MR image (resampled with cubic splines, see figure 2). Middle row: the 3 same slices of the first reconstructed autoradiographic volume registered (affine transformation) against the MR image. Bottom row: the 3 same slices of the last reconstructed autoradiographic volume (after all fusion loops) registered against the MR image.

6 Conclusion

In this paper, we have described a methodology that allows to fuse 2-D sections (autoradiographies) with a 3-D volume (MR). This is done by iterating a so-called *fusion loop* that alternates between the correction of the reconstructed AR volume (by recomputing the 2-D transformations) and a 3-D registration.

Visual inspection of the obtained results is very satisfactory and much more than sufficient for our purpose in the framework of the planned application (comparison of activations detected in autoradiographies to the one detected in fMRI series study).

From a methodological point of view, it should be pointed out that the fusion only involves a stack of 2-D affine transformations and a 3-D affine transformation (no complex 3-D or 2-D elastic transformations are required): we argue that this is appropriate since it faithfully modelizes the acquisition reality.

Now, we still observe some small mismatch areas in our results. Following our strategy, we could perform a last 2-D registration step between AR and corresponding MR sections using transformations with more degrees of freedom. One way would be to use transformations used by [19, 33], and another way would be to design such a transformation by modelizing the specific 2-D distortions which deform the 2-D sections, namely piecewise transformations.

Finally, thanks to the acquisition procedure (the brain and the AR sections are almost always manipulated when frozen), geometrical distortions within an AR section are somehow minimized. It will be challenging to process histological stained data with the same method since, in the later case, strong distortions will certainly occur because of the staining procedure.

Acknowledgments

This work was partially funded by European project MAPAWAMO (ref. QLG3-CT-2000-30161; coordinator: Pr. Guy Orban, Lab. of Neuro- and Psychophysiology, Dept. of Neurosciences and Psychiatry, K.U. Leuven, Belgium). We thank W. Vanduffel, K. Nelissen, D. Fize and G. Orban for providing us with the monkey's autoradiographies and for numerous and stimulating discussions.

References

[1] H. Akaike. An approximation to the density function. *Annals of the Institute of Statistical Mathematics*, 6:127–132, 1954.

[2] P.J. Besl and N.D. McKay. A method for registration of 3-D shapes. *IEEE Transactions on Pattern Analysis and Machine Intelligence*, 14:239–256, February 1992.

[3] Kenneth R. Castleman. *Digital Image Processing*, chapter Point Operations, pages 83–97. Prentice Hall International Editions, 1996.

[4] F.S. Cohen, Z. Yang, Z. Huang, and J. Nissanov. Automatic Matching of Homologous Histological Sections. *IEEE Transaction on Biomedical Engineering*, 45(5):642–649, 1998.

[5] H. Delingette, E. Bardinet, D. Rey, J-D. Lemarechal, J. Montagnat, S. Ourselin, A. Roche, D. Dormont, J. Yelnik, and N. Ayache. Yav++: a software platform for medical image processing and visualization. In *Workshop on Interactive Medical Image Visualization and Analysis satellite symposia of MICCAI, IMIVA'01*, Utrecht, The Netherlands, October 2001.

[6] M.H. Deverell, J.R. Salisbury, M.J. Cookson, J.G. Holman, E. Dykes, and F. Whimster. Three-dimensional reconstruction: methods of improving image registration and interpretation. *Analytical Cellular Pathology*, 5:253–263, 1993.

[7] T.S. Ford-Holevinski, M.R. Castle, J.P. Herman, and S.J. Watson. Microcomputer-based three-dimensional reconstruction of in situ hybridization autoradiographs. *J Chem Neuroanat*, 4(5):373–385, Sep-Oct 1991.

[8] B.J. Geesaman, R.T. Born, R.A. Andersen, and R.B. Tootell. Maps of complex motion selectivity in the superior temporal cortex of the alert macaque monkey: a double-label 2-deoxyglucose study. *Cerebral Cortex*, 7(8):749–757, December 1997.

[9] A.F. Goldszal, O.J. Tretiak, P.J. Hand, S. Bhasin, and D.L. McEachron. Three-dimensional reconstruction of activated columns from 2-[^{14}C]deoxy-D-glucose data. *Neuroimage*, 2(1):9–20, March 1995.

[10] A.F. Goldszal, O.J. Tretiak, D.D. Liu, and P.J. Hand. Multimodality multidimensional image analysis of cortical and subcortical plasticity in the rat brain. *Ann Biomed Eng*, 24(3):430–439, May-June 1996.

[11] A. Hess, K. Lohmann, E.D. Gundelfinger, and H. Scheich. A new method for reliable and efficient reconstruction of 3-dimensional images from autoradiographs of brain sections. *Journal Neurosciences Methods*, 84(1-2):77–86, October 1998.

[12] L.S. Hibbard and R.A. Hawkins. Objective image alignment for three-dimensional reconstruction of digital autoradiograms. *J Neurosci Methods*, 26(1):55–74, November 1988.

[13] C.F. Hildebolt, R.K. Walkup, G.L. Conover, N. Yokoyama-Crothers, T.Q. Bartlett, M.W. Vannier, M.K. Shrout, and J.J. Camp. Histogram-matching and histogram-flattening contrast correction methods: a comparison. *Dentomaxillofac. Radiol.*, 25(1):42–47, 1996.

[14] J.L. Humm, R.M. Macklis, X.Q. Lu, Y. Yang, K. Bump, B. Beresford, and L.M. Chin. The spatial accuracy of cellular dose estimates obtained from 3D reconstructed serial tissue autoradiographs. *Phys Med Biol*, 40(1):163–180, January 1995.

[15] P.A. Kay, R.A. Robb, D.G. Bostwick, and J.J. Camp. Robust 3-D Reconstruction and Analysis of Microstructures from Serial Histologic Sections, with Emphasis on Microvessels in Prostate Cancer. In K. H. Höhne and R. Kikinis, editors, *Visualisation in Biomedical Computing*, volume 1131 of *Lecture Notes in Computer Science*, pages 129–134, Hamburg (Germany), 1996. Springer.

[16] B. Kim, K.A. Frey, S. Mukhopadhyay, B.D. Ross, and C.R. Meyer. Co-Registration of MRI and Autoradiography of Rat Brain in Three-Dimensions Following Automatic Reconstruction of 2D Data Set. In N. Ayache, editor, *Computer Vision, Virtual Reality and Robotics in Medicine*, volume 905 of *Lecture Notes in Computer Science*, pages 262–266, Nice (France), 1995. Springer.

[17] Boklye Kim, Jennifer L. Boes, Kirk A. Frey, and Charles R. Meyer. Mutual information for automated unwarping of rat brain autoradiographs. *Neuroimage*, 5(1):31–40, 1997.

[18] J.B.A. Maintz and M.A. Viergever. A survey of medical image registration. *Medical Image Analysis*, 2(1):1–36, march 1998.

[19] Michael S. Mega, Sylvia S. Chen, Paul M. Thompson, Roger P. Woods, Timur J. Karaca, Abhishek Tiwari, Harry V. Vinters, Gary W. Small, and Arthur W. Toga. Mapping histology to metabolism: Coregistration of stained whole-brain sections to premortem pet in alzheimer's disease. *Neuroimage*, 5(2):147–153, February 1997.

[20] O. Monga, R. Deriche, G. Malandain, and J.-P. Cocquerez. Recursive filtering and edge tracking: two primary tools for 3-D edge detection. *Image and Vision Computing*, 9(4):203–214, August 1991.

[21] M.S. Muthuswamy, P.L. Roberson, R.K. Ten Haken, and D.J. Buchsbaum. A quantitative study of radionuclide characteristics for radioimmunotherapy from 3D reconstructions using serial autoradiography. *Int J Radiat Oncol Biol Phys*, 35(1):165–172, April 1996.

[22] S. Ourselin, A. Roche, G. Subsol, X. Pennec, and N. Ayache. Reconstructing a 3D Structure from Serial Histological Sections. *Image and Vision Computing*, 19(1-2):25–31, January 2001.

[23] Sébastien Ourselin. *Recalage d'images médicales par appariement de régions - Application à la construction d'atlas histologiques 3D*. Thèse de sciences, Université de Nice Sophia-Antipolis, January 2002.

[24] E. Parzen. On the estimation of a probability density function and the mode. *Annals of Mathematical Statistics*, 33:1065–1076, 1962.

[25] X. Pennec and N. Ayache. Uniform distribution, distance and expectation problems for geometric features processing. *Journal of Mathematical Imaging and Vision*, 9(1):49–67, July 1998.

[26] Anand Rangarajan, Haili Chui, Eric Mjolsness, Suguna Pappu, Lila Davachi, Patricia Goldman-Rakic, and James Duncan. A robust point-matching algorithm for autoradiograph alignment. *Medical Image Analysis*, 1(4):379–398, 1997.

[27] A.H. Reisner, C.A. Bucholtz, G.A. Bell, K. Tsui, D. Rosenfeld, and G.T. Herman. Two- and three-dimensional image reconstructions from stained and autoradiographed histological sections. *Comput Appl Biosci*, 6(3):253–261, July 1990.

[28] A. Roche, G. Malandain, and N. Ayache. Unifying Maximum Likelihood Approaches in Medical Image Registration. *International Journal of Imaging Systems and Technology: Special Issue on 3D Imaging*, 11(1):71–80, 2000.

[29] M. Rosenblatt. Remark on some nonparametric estimates of a density function. *Annals of Mathematical Statistics*, 27:832–837, 1956.

[30] Peter J. Rousseuw and Annick M. Leroy. *Robust Regression and Outlier Detection*. Wiley, 1987.

[31] M. Rydmark, T. Jansson, C.H. Berthold, and T. Gustavsson. Computer assisted realignment of light micrograph images from consecutive sections series of cat cerebral cortex. *Journal of Microscopy*, 165:29–47, 1992.

[32] T. Schormann, A. Dabringhaus, and K. Zilles. Statistics of deformations in histology and application to improved alignment with MRI. *IEEE Transactions on Medical Imaging*, 14(1):25–35, March 1995.

[33] T. Schormann and K. Zilles. Three-dimensional linear and nonlinear transformations: an integration of light microscopical and MRI data. *Human Brain Mapping*, 6(5-6):339–347, 1998.

[34] T. Shormann and K. Zilles. Limitation of the Principal Axes Theory. *IEEE Transactions on Medical Imaging*, 16(6):942–947, 1997.

[35] P. Thévenaz, T. Blu, and M. Unser. Interpolation revisited. *IEEE Transactions on Medical Imaging*, 19(7):739–758, July 2000.

[36] P.A. van den Elsen, E.J.D. Pol, and M.A. Viergever. Medical image matching - a review with classification. *IEEE Engineering in Medicine and Biology*, 12(4):26–39, march 1993.

[37] Jan Van Pelt. Hybrid bananas from Leuven. *Flanders*, 53, March-April-May 2002.

[38] W. Vanduffel, R.B. Tootell, and G.A. Orban. Attention-dependent suppression of metabolic activity in the early stages of the macaque visual system. *Cerebral Cortex*, 10(2):109–126, 2000.

[39] W. Vanduffel, R.B. Tootell, A.A. Schoups, and G.A. Orban. The organization of orientation selectivity throughout macaque visual cortex. *Cerebral Cortex*, 12(6):647–662, June 2002.

[40] Z. Zhang. Parameter Estimation Techniques: A Tutorial with Application to Conic Fitting. *Image and Vision Computing Journal*, 15(1):59–76, 1997.

[41] W. Zhao, T.Y. Young, and M.D. Ginsberg. Registration and Three-Dimensional Reconstruction of Autoradiographic Images by the Disparity Analysis Method. *IEEE Transactions on Medical Imaging*, 12(4):782–791, 1993.

Unité de recherche INRIA Sophia Antipolis
2004, route des Lucioles - BP 93 - 06902 Sophia Antipolis Cedex (France)

Unité de recherche INRIA Futurs : Domaine de Voluceau - Rocquencourt - BP 105 - 78153 Le Chesnay Cedex (France)
Unité de recherche INRIA Lorraine : LORIA, Technopôle de Nancy-Brabois - Campus scientifique
615, rue du Jardin Botanique - BP 101 - 54602 Villers-lès-Nancy Cedex (France)
Unité de recherche INRIA Rennes : IRISA, Campus universitaire de Beaulieu - 35042 Rennes Cedex (France)
Unité de recherche INRIA Rhône-Alpes : 655, avenue de l'Europe - 38334 Montbonnot Saint-Ismier (France)
Unité de recherche INRIA Rocquencourt : Domaine de Voluceau - Rocquencourt - BP 105 - 78153 Le Chesnay Cedex (France)

Éditeur
INRIA - Domaine de Voluceau - Rocquencourt, BP 105 - 78153 Le Chesnay Cedex (France)
http://www.inria.fr
ISSN 0249-6399